Applied Physics Letters

RESEARCH ARTICLE | MARCH 18 2024

Quantifying the orbital-to-spin moment ratio under dynamic excitation

Satoru Emori ; Rachel E. Maizel ; Galen T. Street ; Julia L. Jones ; Dario A. Arena ; Padraic Shafer ; Christoph Klewe

Appl. Phys. Lett. 124, 122404 (2024)
https://doi.org/10.1063/5.0198326

AIP Publishing

Applied Physics Letters ARTICLE pubs.aip.org/aip/apl

Quantifying the orbital-to-spin moment ratio under dynamic excitation

Cite as: Appl. Phys. Lett. **124**, 122404 (2024); doi: 10.1063/5.0198326
Submitted: 17 January 2024 · Accepted: 1 March 2024 ·
Published Online: 18 March 2024

Satoru Emori,[1,a)] Rachel E. Maizel,[1] Galen T. Street,[1] Julia L. Jones,[1] Dario A. Arena,[2] Padraic Shafer,[3,b)] and Christoph Klewe[3]

AFFILIATIONS

[1]Department of Physics, Virginia Tech, Blacksburg, Virginia 24060, USA
[2]Department of Physics, University of South Florida, Tampa, Florida 33620, USA
[3]Advanced Light Source, Lawrence Berkeley National Laboratory, Berkeley, California 94720, USA

[a)]**Author to whom correspondence should be addressed:** semori@vt.edu
[b)]**Present address:** National Synchrotron Light Source II, Brookhaven National Laboratory, Upton, New York 11973, USA.

ABSTRACT

The orbital component of magnetization dynamics, e.g., excited by ferromagnetic resonance (FMR), may generate "orbitronic" effects in nanomagnetic devices. Yet, distinguishing orbital dynamics from spin dynamics remains a challenge. Here, we employ x-ray magnetic circular dichroism (XMCD) to quantify the ratio between the orbital and spin components of FMR-induced dynamics in a $Ni_{80}Fe_{20}$ film. By applying the XMCD sum rules at the Ni $L_{3,2}$ edges, we obtain an orbital-to-spin ratio of 0.108 ± 0.005 for the dynamic magnetization. This value is consistent with 0.102 ± 0.008 for the static magnetization, probed with the same x-ray beam configuration as the dynamic XMCD experiment. The demonstrated method presents a possible path to disentangle orbitronic effects from their spintronic counterparts in magnetic media.

Magnetism generally consists of orbital and spin components. Although orbital magnetism is largely quenched in 3*d* transition-metal ferromagnets, it can remain up to ~10% of spin magnetism due to spin–orbit coupling.[1,2] This seemingly small orbital magnetism yields crucial effects for various device applications, such as magnetic anisotropy for perpendicular magnetic recording and Dzyaloshinkii–Moriya interactions for chiral nanomagnetic memories.[3–5] The sum-rule analysis of x-ray magnetic circular dichroism (XMCD) allows for quantifying the orbital moment μ_L and the spin moment μ_S in ferromagnets.[6] From XMCD measurements of static magnetization in a transmission geometry,[7,8] it is typically straightforward to quantify the ratio μ_L/μ_S of the orbital to spin contributions.

When a ferromagnet is excited, e.g., by ferromagnetic resonance (FMR), its dynamic magnetic response also has orbital and spin components. The value of μ_L/μ_S for the dynamic magnetization may not be equal to that for the static magnetization, as the orbital and spin dynamics may be distinct.[9,10] For instance, excited orbital angular momentum could be more strongly coupled to the lattice, thereby leading to stronger dissipation. With a greater dynamic loss of orbital moment than spin moment, μ_L/μ_S for the dynamic magnetization would be smaller than the static counterpart. Indeed, in sub-picosecond demagnetization excited by laser pulses, time-resolved XMCD experiments report a greater reduction in orbital magnetism than spin magnetism.[9,10]

Furthermore, recent studies suggest that FMR in a ferromagnet can pump a flow of nonequilibrium orbital angular momentum into an adjacent "sink" layer or interface.[11–14] Such FMR-driven orbital pumping is predicted to coexist with the well-known spin pumping[15]—and may hold the key to understanding the reportedly large orbitronic effects in nanomagnetic devices.[16–24] The orbital and spin outflows may be absorbed or scattered differently in the sink[25–27] or at the ferromagnet interface.[28,29] Again, if the dynamic orbital loss is stronger (or weaker) than the spin loss, μ_L/μ_S for the FMR-excited dynamic magnetization may be reduced (or increased) compared to the static magnetization. We note that conventional FMR spectroscopy is often used to quantify μ_L/μ_S via the well-known *g*-factor, $(\mu_L/\mu_S)_{\mathrm{FMR}} = (g-2)/2$. However, recent experiments show that $(\mu_L/\mu_S)_{\mathrm{FMR}}$ includes an additional spin-mixing factor and, hence, does not generally equal the true value of μ_L/μ_S.[8] Thus, quantifying μ_L/μ_S with XMCD under *dynamic* excitation is of critical importance for elucidating fundamental angular-momentum dynamics in magnetic materials.

In this Letter, we quantify μ_L/μ_S of FMR-excited dynamic magnetization in a thin film of Permalloy ($Ni_{80}Fe_{20}$). Our focus here is on the magnetism of Ni, which has greater spin–orbit coupling and hence larger μ_L/μ_S at static equilibrium than Fe.[2,8] Moreover, the relatively large spin–orbit splitting of the L_3 and L_2 core level manifolds for Ni (the largest among the elemental 3*d* ferromagnets) facilitates the separation of the XCMD spectral contributions from these core levels. We have conducted XMCD measurements on both static and dynamic Ni magnetizations in the same sample, probed by the same circularly polarized x-ray beam configuration, as illustrated in Fig. 1. Our work presents a unique way to disentangle FMR-driven orbital dynamics from spin dynamics, which may be of interest for testing orbitronic effects in magnetic multilayers.[14,16]

Our film sample was grown by DC magnetron sputtering at a base pressure of 3×10^{-8} Torr and Ar sputtering gas pressure of 3 mTorr. The film stack structure is MgO(substrate)/Ti(3 nm)/Cu (3 nm)/$Ni_{80}Fe_{20}$(30 nm)/Ho(4 nm)/Ti(3 nm). The MgO substrate [MTI Corp, (001)-oriented] allows for luminescence-yield detection of x-ray absorption.[30] Luminescence yield is equivalent to detecting x-ray transmission in the film sample[7] and permits more reliable quantification of μ_L/μ_S, compared to total electron yield and fluorescence yield that are prone to artifacts.[31,32] All film layers were grown with the substrate at room temperature and are hence polycrystalline. The Ti/Cu seed layer is intended to provide higher-quality growth of ferromagnetic films with narrower FMR linewidths.[33] The overlayer of Ho—a rare-earth metal with large orbital magnetism relative to spin magnetism[34]—was intended for examining proximity-induced magnetism at the NiFe/Ho interface and its orbital and spin dynamics. However, we were unable to detect Ho magnetism above the noise level of the XMCD measurements. Hereafter, we exclusively focus on XMCD at the Ni $L_{3,2}$ edges.

All measurements were conducted within the same synchrotron beamtime at room temperature at Beamline 4.0.2 of the Advanced Light Source, Lawrence Berkeley National Laboratory. We carried out both static and dynamic XMCD measurements on the same sample holder, equipped with a photodiode for luminescence yield detection and a coplanar waveguide for driving 2-GHz FMR. In this setup, the sample is mounted with the film immediately adjacent to the waveguide. A 90% circularly polarized x-ray beam illuminates the sample through a tapered ~0.1-mm-diameter hole in the waveguide's center conductor. The incidence angle of the beam was 40° with respect to the film plane, allowing us to detect primarily the magnetization component in the film plane. Further details of the experimental setup are found in Ref. 30. We note that a 2-GHz microwave field was applied during both types of measurements (Fig. 1) to ensure a similar temperature. In the static XMCD experiment, the microwave field was collinear with the equilibrium in-plane magnetization [Fig. 1(a)], so it did not induce FMR. In contrast, the microwave field was orthogonal to the precessional axis to induce FMR in the dynamic XMCD experiment [Fig. 1(b)].

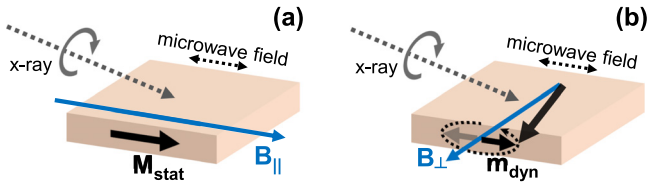

FIG. 1. Schematic illustrations of (a) the static XMCD experiment to probe the static magnetization, $\mathbf{M}_{stat}$, and (b) the dynamic XMCD experiment to measure the dynamic magnetization, $\mathbf{m}_{dyn}$.

We first demonstrate our static XMCD result for quantifying μ_L/μ_S of the Ni magnetization at equilibrium. The x-ray photon energy was stepped discretely from 820 to 909 eV to acquire x-ray absorption spectra (XAS). At each energy setpoint, the static magnetic field, $B_{||}$, was alternated between +0.3 and −0.3 T along the incident x-ray beam axis. The circular polarization of the x-ray beam was fixed. To enhance the signal-to-noise ratio, we averaged 23 pairs of XAS scans.

The x-ray transmission intensity was normalized, and the linear background [Fig. 2(a) inset] was subtracted to produce the spectra in Fig. 2(a), following the method explained in the supplementary material. The normalized transmitted x-ray intensity I is converted to the x-ray absorption $A = -\ln(I)$. Figure 2(b) shows the resulting XAS for $B_{||} = +0.3$ and −0.3 T. By taking the difference between the XAS at the two opposite magnetization directions, the static XMCD spectrum in Fig. 2(c) was obtained. In producing the XMCD spectrum, we

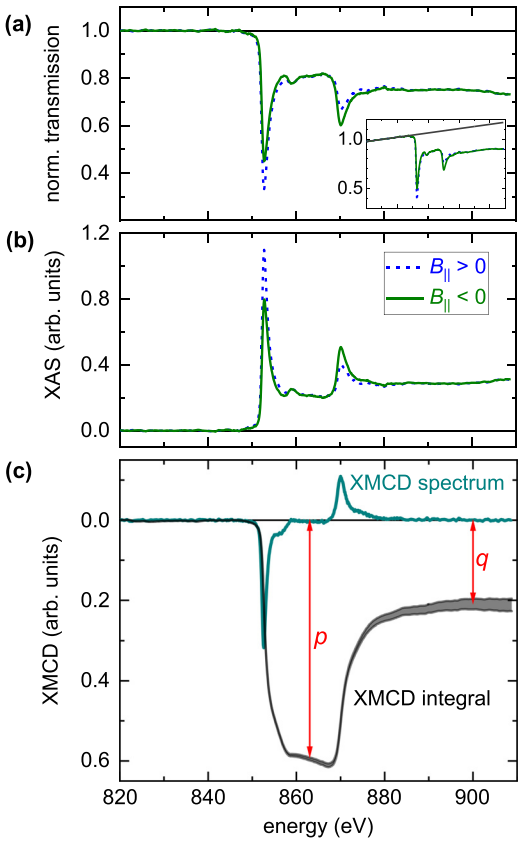

FIG. 2. (a) Normalized x-ray transmission (measured via luminescence yield) and (b) x-ray absorption spectra (XAS) under the opposite directions of the static applied field $B_{||}$. Inset of (a): normalized x-ray transmission before subtracting the linear background. (c) Static XMCD spectrum, obtained from the difference between the two XAS spectra in (b), along with the integrated XMCD curve and the parameters *p* and *q* used in Eq. (1).

performed post-edge normalization described in the supplementary material.

The ratio between the orbital moment μ_L and spin moment μ_S is computed with the standard XMCD sum-rule formula:

$$\frac{\mu_L}{\mu_S^{\text{eff}}} \approx \frac{\mu_L}{\mu_S} = \frac{2}{3}\left(\frac{q}{3p-2q}\right), \quad (1)$$

where q is the value of the integrated XMCD spectrum across the L_3 and L_2 edges, whereas p is the value of the integrated XMCD spectrum across only the L_3 edge.[6] Figure 2(c) shows the integrated XMCD spectrum and the definitions of q and p. Here, q is obtained in the post-edge energy range (explained in the supplementary material), and p is obtained using the cutoff energy of 863 eV that delineates the L_3 and L_2 core level manifolds. Strictly speaking, the denominator in Eq. (1) is the "effective" spin moment $\mu_S^{\text{eff}} = \mu_S - 7\langle T_z\rangle\mu_B/\hbar$ that includes the expectation value of the magnetic dipole operator $\langle T_z\rangle$. The $7\langle T_z\rangle$ term can exceed a few percent of μ_S in atomically thin 3d ferromagnets, but it diminishes to an undetectable level when the 3d ferromagnet thickness is several atomic monolayers or greater.[8,35,36] In our present 30-nm-thick Permalloy film, we safely assume that $\mu_S^{\text{eff}} = \mu_S$.

From the static XMCD experiment, we arrive at an orbital-to-spin ratio of $\mu_L/\mu_S \approx 0.102$ by applying Eq. (1). This value is comparable to the typical μ_L/μ_S of ~0.1 for Ni in Permalloy in recent XMCD experiments.[8,37] We identify an uncertainty of ± 0.008 for μ_L/μ_S due to the variation in the outcome of the post-edge normalization (see the supplementary material). This uncertainty is graphically represented as a shaded band in Fig. 2(c).

We now describe our time-resolved dynamic XMCD experiment, with the sample magnetized by the external field $B_\perp$ orthogonal to the x-ray beam [Fig. 1(b)]. The magnetization was excited by a 2-GHz microwave field and precesses about $B_\perp$. The circularly polarized x-ray beam probed the FMR-induced dynamics of the nonequilibrium magnetization [$\mathbf{m}_{\text{dyn}}$ in Fig. 1(b)]. Similar to the normalization of the static transmission signal (described in the supplementary material), the dynamic transmission signal acquired via lock-in detection[30] was normalized by the incident beam intensity upstream at the end station detector of the beamline.

Figure 3(a) shows time traces of the dynamic differential x-ray transmission signal obtained at a fixed photon energy of 852.8 eV and different $B_\perp$, employing the phase-modulated lock-in protocol outlined in Refs. 30 and 38. These traces are fit excellently by sinusoids with an oscillation period of 500 ps, as expected from the 2-GHz microwave excitation. From each fit, we extract both the amplitude and phase of the dynamic magnetization. Figures 3(b) and 3(c) reveal a peak in the amplitude and a 180° shift in the phase, which are consistent with FMR.[39–41] The resonance field $B_{\text{res}} \approx 4.5$ mT is obtained by fitting the $B_\perp$ dependence of the amplitude with $\propto \sqrt{\Delta B^2/(\Delta B^2 + (B_\perp - B_{\text{res}})^2)}$ and that of the phase with $\phi_o + \text{atan}(\Delta B/(B_\perp - B_{\text{res}}))$. The fits also yield the FMR linewidth, $\Delta B \approx 1.0$ mT; the phase offset ϕ_o from the experimental setup is shifted to 0 in Fig. 3(c) for clarity.

To quantify μ_L/μ_S for the dynamic magnetization, it is necessary to measure the energy dependence of the dynamic XMCD signal. All following measurements were performed at $B_\perp = B_{\text{res}}$ to maximize the signal amplitude. As shown in Fig. 4(a), time traces of differential x-ray transmission reveal sinusoidal oscillations. All have the same

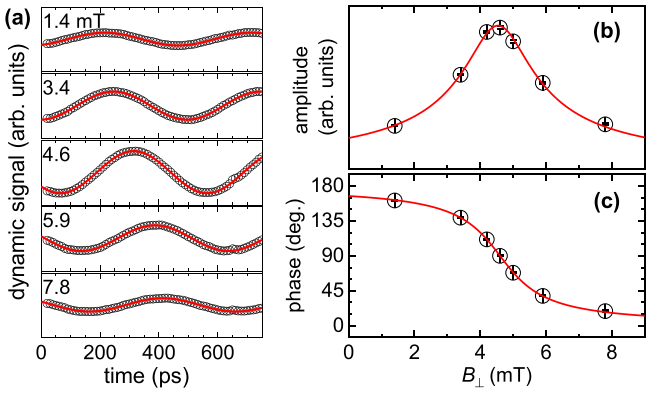

FIG. 3. (a) Time traces of the differential dynamic x-ray transmission signal, arising from FMR-induced magnetization oscillations, at several values of applied field $B_\perp$ [orthogonal to the x-ray beam axis, see Fig. 1(a)]. The photon energy is fixed at the peak of the Ni L_3 edge. (b) and (c) $B_\perp$ dependence of the precessional (b) amplitude and (c) phase. The symbols are the values derived from the measurements. The red curves represent the best fits, from which the resonance field $B_{\text{res}} \approx 4.5$ mT is quantified.

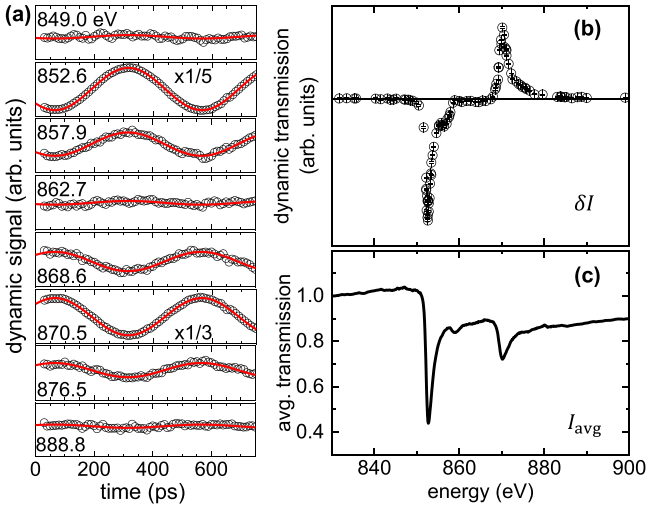

FIG. 4. (a) Time traces of the differential dynamic x-ray transmission signal, arising from FMR-induced magnetization oscillations, at several values of photon energy. The field $B_\perp$ is fixed at $B_{\text{res}} = 4.5$ mT. (b) and (c) Energy dependence of (b) the amplitude of the differential x-ray transmission, δI, and (c) the equilibrium average x-ray transmission, I_{avg}, derived from the average of the two curves in the inset of Fig. 2(a).

period of 500 ps, but the phase exhibits a discrete 180° shift, corresponding to the sign of the static XMCD signal at that energy (e.g., compare 852.6 eV near the L_3 edge maximum amplitude with 870.5 eV near the L_2 edge maximum). By plotting the energy dependence of the oscillation amplitude [Fig. 4(b)], we observe a trend that resembles the XMCD spectrum for the static magnetization [Fig. 2(c)].

Yet, caution must be taken before applying the XMCD sum rules. What is shown in Fig. 4(b) is the amplitude of the measured differential x-ray *transmission*, $\delta I = I^- - I^+$, between the dynamic

magnetization oriented parallel (I^+) and antiparallel (I^-) to the incident beam. To analyze dynamic XMCD properly, δI must be converted to the differential x-ray *absorption*

$$\delta A = \ln(I^+) - \ln(I^-). \tag{2}$$

Since the precessional cone angle here is only ~1°, δI is a small perturbation about the average transmission I_{avg}, such that $I^{\pm} = I_{avg} \pm \delta I/2$ with $\delta I \ll I_{avg}$. Then, we can re-write Eq. (2) as

$$\delta A = \ln\left(1 + \frac{\delta I}{2I_{avg}}\right) - \ln\left(1 - \frac{\delta I}{2I_{avg}}\right) \approx \frac{\delta I}{I_{avg}}. \tag{3}$$

We take I_{avg} from Fig. 4(c), which is the average of the static transmission spectra at $B_{\parallel} > 0$ and < 0 [inset of Fig. 2(a)]. The resulting dynamic XMCD amplitude δA obtained from Eq. (3) is presented in Fig. 5(a). This analysis protocol is crucial for deriving an accurate dynamic XMCD spectrum; applying the XMCD sum rules on δI vs energy [Fig. 4(b)] would result in an incorrect estimation of μ_L/μ_S. We also remark that, in principle, I_{avg} can be obtained from the DC luminescence yield signal acquired simultaneously with the dynamic signal. However, in practice, our detection electronics (optimized for the dynamic luminescence yield signal) did not produce a sufficient signal-to-noise ratio for the DC signal, such that I_{avg} needed to be obtained from a separate set of static measurements (Fig. 2).

Figure 5 is the central result of this study. Figure 5(a) reveals that the dynamic XMCD data closely track the static XMCD spectrum. This close correspondence already suggests that μ_L/μ_S is similar for the dynamic magnetization and the static magnetization. Furthermore, comparing the XMCD integrals for the dynamic and static cases in Fig. 5(b) again reveals close agreement.

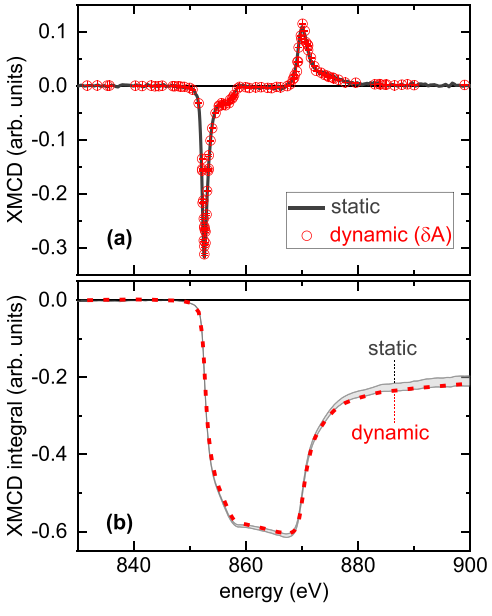

FIG. 5. Energy dependence of (a) the static and dynamic XMCD amplitudes and (b) the XMCD integrals. The dynamic XMCD data (δA) are derived by applying Eq. (3) to the data shown in Figs. 4(b) and 4(c).

Nevertheless, by applying the sum-rule analysis [Eq. (1)] to the dynamic XMCD integral, we obtain $(\mu_L/\mu_S)_{dyn} \approx 0.108$. This value is noticeably higher than the mean $(\mu_L/\mu_S)_{stat} \approx 0.102$ for the static magnetization. The possibility that $(\mu_L/\mu_S)_{dyn} > (\mu_L/\mu_S)_{stat}$ would suggest stronger dissipation for spin dynamics than orbital dynamics. This is contrary to the intuitive expectation of stronger orbital dissipation by the more direct orbital-to-lattice coupling. A potential explanation is that the thin Ho layer, interfaced with the Permalloy film, more efficiently absorbs FMR-pumped nonequilibrium spin angular momentum than orbital angular momentum.

However, from our present XMCD results alone, we are unable to conclude that dynamic spin dissipation is stronger than orbital dissipation—or that $(\mu_L/\mu_S)_{dyn}$ is higher than $(\mu_L/\mu_S)_{stat}$. Considering the uncertainty in q due to the limited post-edge data density for the dynamic XMCD, the uncertainty in $(\mu_L/\mu_S)_{dyn}$ may be up to ± 0.005. Taking into account for the uncertainties in our static and dynamic XMCD results, we have $(\mu_L/\mu_S)_{dyn} = 0.108 \pm 0.005$ and $(\mu_L/\mu_S)_{stat} = 0.102 \pm 0.008$—i.e., the values of $(\mu_L/\mu_S)_{dyn}$ and $(\mu_L/\mu_S)_{stat}$ are indistinguishable. Moreover, there are conceivably additional sources of uncertainty for $(\mu_L/\mu_S)_{stat}$, as the setup here was optimized for dynamic XMCD but not for static XMCD. For instance, the substrate may have an energy-dependent luminescence yield background[7] that distorts the XAS spectrum, although it is yet unclear how this may affect the XMCD spectrum; the influence of such a substrate-dependent background may be investigated in future experiments. Despite the extended averaging, our derived $(\mu_L/\mu_S)_{stat}$ may also be affected by small fluctuations of the static XMCD measurements. Considering the points above, $(\mu_L/\mu_S)_{stat}$ and $(\mu_L/\mu_S)_{dyn}$ are essentially identical within experimental uncertainty for this particular sample.

In summary, we have employed XMCD to quantify the orbital-to-spin ratio μ_L/μ_S of FMR-excited dynamic magnetization in a Permalloy film. This dynamic μ_L/μ_S ratio turns out to agree closely with its static counterpart to within a few percent. Our present results cannot determine conclusively whether FMR-driven orbital dynamics differs from spin dynamics. Nevertheless, in future studies, experimental uncertainties may be tightened for a more precise quantification of μ_L/μ_S. Future work will also benefit from studying a series of samples with different compositions and layer structures. A systematic relative variation in the dynamic μ_L/μ_S ratio among these samples may uncover orbital dissipation that is distinct from its spin counterpart.[26–29] Moreover, the dynamic XMCD method may allow for resolving the variation of μ_L/μ_S during magnetic precession[42] in a highly anisotropic, single-crystalline magnetic film, whose orbital magnetism is strongly linked to the crystal orientation. Such time-resolved mapping of μ_L/μ_S may provide direct insight into the breathing Fermi surface mechanism that governs intrinsic magnetic damping.[43,44] Overall, our unique approach provides an avenue for quantitatively evaluating dynamic orbital-based effects—beyond the conventional spin-based picture—in nanomagnetic structures.

See the supplementary material for additional information on the post-edge normalization of the static XMCD spectrum.

S.E. and G.T.S. were supported by the Air Force Office of Scientific Research under Grant No. FA9550-21-1-0365. R.E.M. and

J.L.J. were supported by the National Science Foundation under No. ENG-ECCS-2144333. D.A.A. acknowledges the support from the National Science Foundation under Grant No. ENG-ECCS-1952957. P.S. and C.K. acknowledge the partial support from the U.S. Department of Energy, Office of Science, Office of Basic Energy Sciences, Materials Sciences and Engineering Division under Contract No. DE-AC02-05-CH11231 (Codesign of Ultra-Low-Voltage Beyond CMOS Microelectronics for the development of materials for low-power microelectronics). This research used resources of the Advanced Light Source, which is a DOE Office of Science User Facility under Contract No. DE-AC02-05CH11231.

AUTHOR DECLARATIONS

Conflict of Interest

The authors have no conflicts to disclose.

Author Contributions

Satoru Emori: Conceptualization (equal); Data curation (lead); Formal analysis (lead); Funding acquisition (lead); Investigation (equal); Methodology (equal); Project administration (lead); Resources (supporting); Software (equal); Supervision (lead); Visualization (lead); Writing – original draft (lead); Writing – review & editing (lead). **Rachel E. Maizel:** Formal analysis (supporting); Investigation (equal); Software (supporting); Supervision (supporting); Writing – review & editing (supporting). **Galen T. Street:** Formal analysis (supporting); Investigation (equal); Writing – review & editing (supporting). **Julia L. Jones:** Formal analysis (supporting); Investigation (equal). **Dario A. Arena:** Conceptualization (equal); Formal analysis (supporting); Funding acquisition (supporting); Methodology (supporting); Writing – review & editing (equal). **Padraic Shafer:** Funding acquisition (supporting); Methodology (supporting); Resources (equal); Writing – review & editing (equal). **Christoph Klewe:** Investigation (equal); Methodology (equal); Resources (equal); Writing – review & editing (equal).

DATA AVAILABILITY

The data that support the findings of this study are available from the corresponding author upon reasonable request.

REFERENCES

[1]R. C. O'Handley, *Modern Magnetic Materials: Principles and Applications* (Wiley-Interscience, 1999).
[2]M. A. W. Schoen, J. Lucassen, H. T. Nembach, T. J. Silva, B. Koopmans, C. H. Back, and J. M. Shaw, Phys. Rev. B **95**, 134410 (2017).
[3]B. Dieny and M. Chshiev, Rev. Mod. Phys. **89**, 025008 (2017).
[4]J. Okabayashi, J. W. Koo, H. Sukegawa, S. Mitani, Y. Takagi, and T. Yokoyama, Appl. Phys. Lett. **105**, 122408 (2014).
[5]S. Kim, K. Ueda, G. Go, P.-H. Jang, K.-J. Lee, A. Belabbes, A. Manchon, M. Suzuki, Y. Kotani, T. Nakamura, K. Nakamura, T. Koyama, D. Chiba, K. T. Yamada, D.-H. Kim, T. Moriyama, K.-J. Kim, and T. Ono, Nat. Commun. **9**, 1648 (2018).
[6]C. T. Chen, Y. U. Idzerda, H. J. Lin, N. V. Smith, G. Meigs, E. Chaban, G. H. Ho, E. Pellegrin, and F. Sette, Phys. Rev. Lett. **75**, 152 (1995).
[7]C. Piamonteze, Y. W. Windsor, S. R. Avula, E. Kirkc, and U. Staub, J. Synchrotron Radiat. **27**, 1289 (2020).
[8]J. M. Shaw, R. Knut, A. Armstrong, S. Bhandary, Y. Kvashnin, D. Thonig, E. K. Delczeg-Czirjak, O. Karis, T. J. Silva, E. Weschke, H. T. Nembach, O. Eriksson, and D. A. Arena, Phys. Rev. Lett. **127**, 207201 (2021).
[9]C. Boeglin, E. Beaurepaire, V. Halté, V. López-Flores, C. Stamm, N. Pontius, H. A. Dürr, and J. Y. Bigot, Nature **465**(7297) 458–461 (2010).
[10]N. Bergeard, V. López-Flores, V. Halté, M. Hehn, C. Stamm, N. Pontius, E. Beaurepaire, and C. Boeglin, Nat. Commun. **5**, 3466 (2014).
[11]E. Santos, J. Abrão, D. Go, L. de Assis, Y. Mokrousov, J. Mendes, and A. Azevedo, Phys. Rev. Appl. **19**, 014069 (2023).
[12]A. El Hamdi, J. Y. Chauleau, M. Boselli, C. Thibault, C. Gorini, A. Smogunov, C. Barreteau, S. Gariglio, J. M. Triscone, and M. Viret, Nat. Phys. **19**, 1855–1860 (2023).
[13]H. Hayashi, D. Go, Y. Mokrousov, and K. Ando, arXiv:2304.05266 (2023).
[14]D. Go, K. Ando, A. Pezo, S. Blügel, A. Manchon, and Y. Mokrousov, arXiv:2309.14817 (2023).
[15]Y. Tserkovnyak, A. Brataas, G. E. W. Bauer, and B. I. Halperin, Rev. Mod. Phys. **77**, 1375 (2005).
[16]D. Go, D. Jo, H. W. Lee, M. Kläui, and Y. Mokrousov, Europhys. Lett. **135**, 37001 (2021).
[17]S. Ding, A. Ross, D. Go, L. Baldrati, Z. Ren, F. Freimuth, S. Becker, F. Kammerbauer, J. Yang, G. Jakob, Y. Mokrousov, and M. Kläui, Phys. Rev. Lett. **125**, 177201 (2020).
[18]D. Lee, D. Go, H. J. Park, W. Jeong, H. W. Ko, D. Yun, D. Jo, S. Lee, G. Go, J. H. Oh, K. J. Kim, B. G. Park, B. C. Min, H. C. Koo, H. W. Lee, O. J. Lee, and K. J. Lee, Nat. Commun. **12**(1), 6710 (2021).
[19]C. Y. Hu, Y. F. Chiu, C. C. Tsai, C. C. Huang, K. H. Chen, C. W. Peng, C. M. Lee, M. Y. Song, Y. L. Huang, S. J. Lin, and C. F. Pai, ACS Appl. Electron. Mater. **4**, 1099 (2022).
[20]A. Rothschild, N. Am-Shalom, N. Bernstein, M. Meron, T. David, B. Assouline, E. Frohlich, J. Xiao, B. Yan, and A. Capua, Phys. Rev. B **106**, 144415 (2022).
[21]H. Hayashi, D. Jo, D. Go, T. Gao, S. Haku, Y. Mokrousov, H.-W. Lee, and K. Ando, Commun. Phys. **6**(1), 32 (2023).
[22]Y. G. Choi, D. Jo, K. H. Ko, D. Go, K. H. Kim, H. G. Park, C. Kim, B. C. Min, G. M. Choi, and H. W. Lee, Nature **619**(7968), 52–56 (2023).
[23]I. Lyalin, S. Alikhah, M. Berritta, P. M. Oppeneer, and R. K. Kawakami, Phys. Rev. Lett. **131**, 156702 (2023).
[24]G. Sala, H. Wang, W. Legrand, and P. Gambardella, Phys. Rev. Lett. **131**, 156703 (2023).
[25]G. Sala and P. Gambardella, Phys. Rev. Res. **4**, 033037 (2022).
[26]D. Go, D. Jo, K. W. Kim, S. Lee, M. G. Kang, B. G. Park, S. Blügel, H. W. Lee, and Y. Mokrousov, Phys. Rev. Lett. **130**, 246701 (2023).
[27]A. Manchon, A. Pezo, K.-W. Kim, and K.-J. Lee, arXiv:2310.04763v1 (2023).
[28]K. D. Belashchenko, G. G. B. Flores, W. Fang, A. A. Kovalev, M. van Schilfgaarde, P. M. Haney, and M. D. Stiles, Phys. Rev. B **108**, 144433 (2023).
[29]S. Urazhdin, Phys. Rev. B **108**, L180404 (2023).
[30]C. Klewe, Q. Li, M. Yang, A. T. N'Diaye, D. M. Burn, T. Hesjedal, A. I. Figueroa, C. Hwang, J. Li, R. J. Hicken, P. Shafer, E. Arenholz, G. van der Laan, and Z. Qiu, Synchrotron Radiat. News **33**, 12 (2020).
[31]R. Nakajima, J. Stöhr, and Y. U. Idzerda, Phys. Rev. B **59**, 6421 (1999).
[32]B. Liu, C. Piamonteze, M. U. Delgado-Jaime, R. P. Wang, J. Heidler, J. Dreiser, R. Chopdekar, F. Nolting, and F. M. D. Groot, Phys. Rev. B **96**, 054446 (2017).
[33]E. R. Edwards, H. T. Nembach, and J. M. Shaw, Phys. Rev. Appl. **11**, 054036 (2019).
[34]S. G. Reidy, L. Cheng, and W. E. Bailey, Appl. Phys. Lett. **82**, 1254 (2003).
[35]M. Gottwald, S. Andrieu, F. Gimbert, E. Shipton, L. Calmels, C. Magen, E. Snoeck, M. Liberati, T. Hauet, E. Arenholz, S. Mangin, and E. E. Fullerton, Phys. Rev. B **86**, 014425 (2012).
[36]S. Andrieu, T. Hauet, M. Gottwald, A. Rajanikanth, L. Calmels, A. M. Bataille, F. Montaigne, S. Mangin, E. Otero, P. Ohresser, P. L. Fèvre, F. Bertran, A. Resta, A. Vlad, A. Coati, and Y. Garreau, Phys. Rev. Mater. **2**, 064410 (2018).
[37]B. Glaubitz, S. Buschhorn, F. Brüssing, R. Abrudan, and H. Zabel, J. Phys.: Condens. Matter **23**, 254210 (2011).
[38]D. A. Arena, E. Vescovo, C.-C. Kao, Y. Guan, and W. E. Bailey, Phys. Rev. B **74**, 064409 (2006).

[39]Y. Guan, W. Bailey, E. Vescovo, C.-C. Kao, and D. Arena, J. Magn. Magn. Mater. **312**, 374 (2007).
[40]J. Li, L. R. Shelford, P. Shafer, A. Tan, J. X. Deng, P. S. Keatley, C. Hwang, E. Arenholz, G. van der Laan, R. J. Hicken, and Z. Q. Qiu, Phys. Rev. Lett. **117**, 076602 (2016).
[41]A. A. Baker, A. I. Figueroa, C. J. Love, S. A. Cavill, T. Hesjedal, and G. van der Laan, Phys. Rev. Lett. **116**, 047201 (2016).
[42]D. A. Arena, Y. Ding, E. Vescovo, S. Zohar, Y. Guan, and W. E. Bailey, Rev. Sci. Instrum. **80**, 83903 (2009).
[43]K. Gilmore, Y. U. Idzerda, and M. D. Stiles, Phys. Rev. Lett. **99**, 027204 (2007).
[44]B. Khodadadi, A. Rai, A. Sapkota, A. Srivastava, B. Nepal, Y. Lim, D. A. Smith, C. Mewes, S. Budhathoki, A. J. Hauser, M. Gao, J.-F. Li, D. D. Viehland, Z. Jiang, J. J. Heremans, P. V. Balachandran, T. Mewes, and S. Emori, Phys. Rev. Lett. **124**, 157201 (2020).